INTERNATIONAL JOURNAL OF HYDROGEN ENERGY 40 (2015) 7895–7902

Available online at www.sciencedirect.com

ScienceDirect

journal homepage: www.elsevier.com/locate/he

# Micro level two dimensional stress and thermal analysis anode/electrolyte interface of a solid oxide fuel cell

Selahattin Celik [a,*], Beycan Ibrahimoglu [b], Mahmut D. Mat [c], Yuksel Kaplan [a], T. Nejat Veziroglu [d]

[a] Nigde University, Mechanical Engineering Department, 51245, Nigde, Turkey
[b] Abdullah Gul University, Mechanical Engineering Department, 38039, Kayseri, Turkey
[c] Meliksah University, Mechanical Engineering Department, 38280, Kayseri, Turkey
[d] International Association for Hydrogen Energy, Miami University, Miami, USA

ARTICLE INFO

*Article history:*
Received 4 August 2014
Received in revised form
25 September 2014
Accepted 13 October 2014
Available online 2 November 2014

*Keywords:*
Solid oxide fuel cell
Micro level modeling
Stress analysis
SOFC anode
Overpotential

ABSTRACT

The delamination and degradation of solid oxide fuel cells (SOFCs) electrode/electrolyte interface is estimated by calculating the stresses generated within the different layers of the cell. The stresses developed in a SOFC are usually assumed to be homogenous through a cross section in the mathematical models at macroscopic scales. However, during the operating of these composite materials the real stresses on the multiphase porous layers might be very different than those at macro-scale. Therefore micro-level modeling is needed for an accurate estimation of the real stresses and the performance of SOFC.

This study combines the microstructural characterization of a porous solid oxide fuel cell anode/electrolyte with two dimensional mechanical and electrochemical analyses to investigate the stress and the overpotential. The microstructure is determined by using focused ion beam (FIB) tomography and the resulting microstructures are used to generate a solid mesh of two dimensional triangular elements. COMSOL Multiphysics package is employed to calculate the principal stress and Maxwell Stefan Diffusion. The stress field is calculated from room temperature to operating temperature while the overpotential is calculated at operating temperature.



## Introduction

Solid oxide fuel cells (SOFCs) are considered as one of the most promising system for the energy vision of the future in the view of the fuel flexibility, high conversion efficiency, low emission and cheap raw materials [1]. Many researches have focused enhancing the service life of SOFCs and to reduce fuel cell costs [2]. One of the most

* Corresponding author. Tel.: +90 388 225 24 50; fax: +90 388 225 01 12.
E-mail address: scelik@nigde.edu.tr (S. Celik).
http://dx.doi.org/10.1016/j.ijhydene.2014.10.057

essential parameters that needs to be considered is the high operating temperature which leads to delamination of the cell component and the degradation of the cell performance. A typical SOFC comprises anode electrode, electrolyte and cathode electrode layers. Each of these layers are consistent of different materials. In addition to these layers a certain amount of electrolyte material is generally added to both electrodes in order to improve the cell performance by increasing the electrochemical reaction zones known as triple phase boundaries. Therefore, all layers exhibit different mechanical properties such as elasticity modulus, Poison's ratio and coefficient of thermal expansions (CTE). The mechanical properties are also not homogenous in both electrodes because of the electrolyte materials added. The CTE differences between each layers and in anode and cathode microstructures lead to micro or macro cracks at the layer interfaces and inside the electrodes. This problem alleviates at high temperature gradient during the operation of SOFC [3]. Especially, in CTE causes additional stresses in the electrode/electrolyte interfaces and the grains in electrode. Since the SOFC systems include many electrochemical reactions and mechanical enforcements due to the assembly features, understanding of the initiation of the defects and their reasons are quite essential.

Recently, studies investigating about the reasons of the defects in the micro scale have been increased with the developments in the visualization techniques of microstructures. For this purpose generally advanced focused ion beam (FIB)–scanning electron microscopy (SEM) [4–11] and X-ray computed tomography (XCT) [12,13] devices are utilized in order to obtain the representative volume element (RVE) which will be used in the finite element simulations later. Although these kinds of detailed visualization techniques are new, its application to SOFC microstructure have been increasing remarkably.

In the current study, the generated microstructures are used for the determination of the interactions between Ni and YSZ phases as well as the stress distributions and delamination features of the electrode/electrolyte interfaces in a range of SOFC operating temperatures.

## Microstructure generation

There are numerous 1D, 2D and 3D fuel cell modeling studies in the literature. With the recent developments in the visualization equipment, it is now possible to scanning microstructures layer by layer. Furthermore, 2D and 3D images of the cross-section of solid oxide fuel cells obtained by using these visualization devices have been numerically analyzed. Considered 2D SEM image of anode/electrolyte interface belonging to a membrane electrode group is given in Fig. 1 [14]. The coloring of this image is achieved via a commercial image analysis program (Image-Pro Plus v60.0.1). Before implementing into COMSOL program, the colored image is converted to high quality image data and dxf (drawing exchange format) sequentially (Fig. 2). The meshed structure of the geometry of interest obtained in COMSOL is illustrated in Fig. 3. In order to obtain more accurate results, relatively small and high numbers of meshes are applied for the sharp edges as well as contact regions. The statistical values of the mesh structure are listed in Table 1.

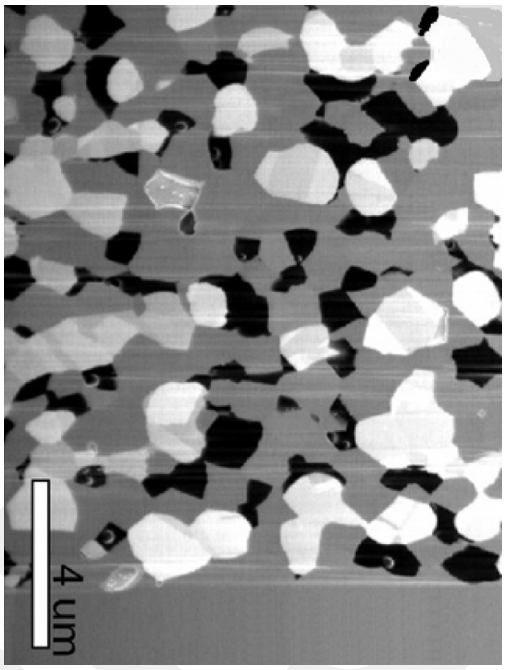


**Fig. 1 – Anode/electrolyte cross section obtained by FIB–SEM [13].**

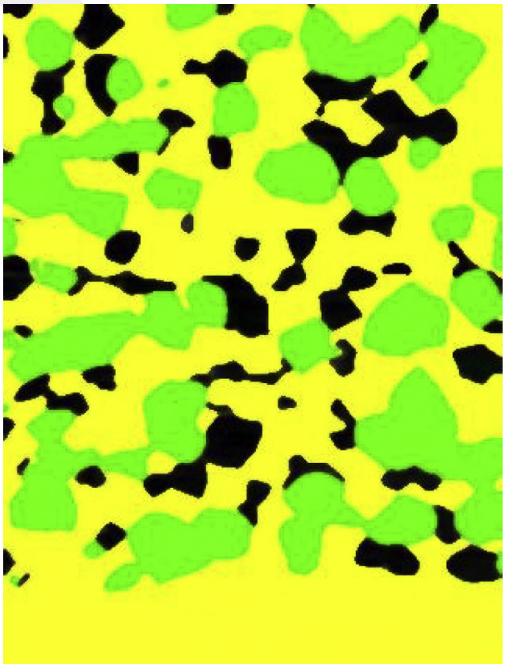

**Fig. 2 – Colored anode/electrolyte cross section with segmentation (Green: Nickel, Yellow: YSZ, Black: Pores). (For interpretation of the references to colour in this figure legend, the reader is referred to the web version of this article.)**

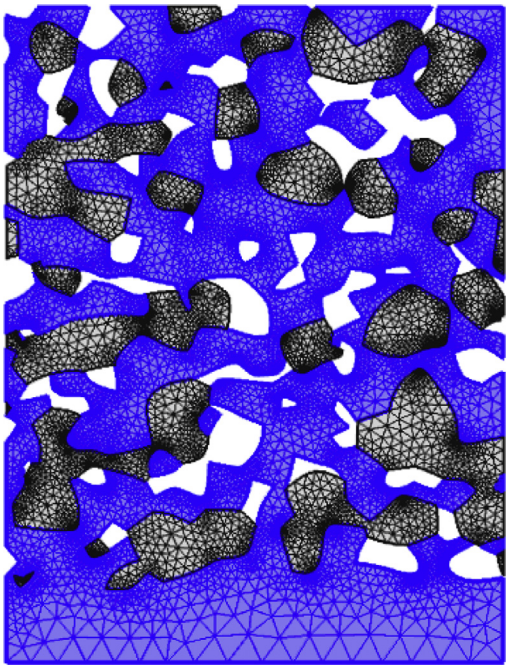

**Fig. 3 – Meshed anode/electrolyte cross section with Comsol (Gray: Nickel, Blue: YSZ, White: Pores). (For interpretation of the references to colour in this figure legend, the reader is referred to the web version of this article.)**

## Mathematical model

### *Thermo mechanic strain–stress equations*

The displacement and stress generation due to thermal expansion mismatch are considered. Energy generation as a result of electrochemical reaction is neglected because of very small volume of computational domain chosen. The force balance for the solid body element in its differential form states [15]:

$$\frac{\partial^2(\rho \boldsymbol{u})}{\partial t^2} - \nabla\cdot\sigma = \rho \boldsymbol{f} \tag{1}$$

where $\boldsymbol{u}$ is displacement vector, $\rho$ is density, $\boldsymbol{f}$ is body force and $\sigma$ is stress tensor.

The strain tensor $\varepsilon$ is defined in terms of $\boldsymbol{u}$:

**Table 1 – Statistical data of mesh specification.**

| Specification | Numbers |
|---|---|
| The number of the triangular elements | 24,342 |
| The number of edge element | 2586 |
| The number of the corner element | 453 |
| Total number of elements | 24,342 |
| Minimum elements of quality | 0.1372 |
| Average elements quality | 0.9343 |
| Element area ratio | 4.12E−4 |
| Network area | 22.71 μm$^2$ |

$$\varepsilon = \frac{1}{2}\left[\nabla \boldsymbol{u} + (\nabla \boldsymbol{u})^T\right] \tag{2}$$

The Hooke's law, relating the stress and strain tensor, closes the system of equations:

$$\sigma = 2\mu\varepsilon + \lambda \mathrm{tr}(\varepsilon)\boldsymbol{I} \tag{3}$$

where tr($\varepsilon$) is the transpose of the strain tensor, $\boldsymbol{I}$ is the unit tensor and $\mu$ and $\lambda$ Lame's coefficients, relating to Young's modulus of elasticity $E$ and Poisson's ratio $\upsilon$ as:

$$\mu = \frac{E}{2(1+\upsilon)} \tag{4}$$

and

$$\lambda = \begin{cases} \dfrac{\upsilon E}{(1+\upsilon)(1-\upsilon)} & \text{for plane stress} \\ \dfrac{\upsilon E}{(1+\upsilon)(1-2\upsilon)} & \text{for plane strain and 3D} \end{cases} \tag{5}$$

There are well-known relationships between stress and displacement, and for plane stress with possible temperature loading [16];

$$\sigma_{xx} = \frac{E}{(1-\mu^2)}\left\{\frac{\partial u}{\partial x} + \mu\frac{\partial \upsilon}{\partial y} - (1+\mu)\alpha T\right\} \tag{6}$$

$$\sigma_{yy} = \frac{E}{(1-\mu^2)}\left\{\frac{\partial \upsilon}{\partial y} + \mu\frac{\partial u}{\partial yx} - (1+\mu)\alpha T\right\} \tag{7}$$

$$\sigma_{xy} = \frac{E}{2(1+\mu)}\left\{\frac{\partial u}{\partial y} + \frac{\partial \upsilon}{\partial x}\right\} \tag{8}$$

Using the equations above, the governing equation can be rewritten with the displacement vector $\boldsymbol{u}$ as the primitive variable [15]:

$$\frac{\partial^2(\rho \boldsymbol{u})}{\partial t^2} - \nabla\cdot\left[\mu\nabla \boldsymbol{u} + (\nabla \boldsymbol{u})^T + \lambda \mathrm{I}\mathrm{tr}(\nabla \boldsymbol{u})\right] = \rho \boldsymbol{f} \tag{9}$$

### *Continuity equation*

The continuity equation for the all of domains of a single cell i.e. the anode, the cathode, the electrolyte, the interconnectors and gas channels are given;

$$\frac{\partial(\varepsilon\rho)}{\partial t} + \nabla\cdot(\rho\vec{V}) = \sum R_j \tag{10}$$

Where, $\varepsilon$ is the porosity correction for the electrodes. In the anode and cathode, source terms are prescribed in the continuity equation to take into account of homogenous reactions. In the cathode, oxygen is consumed and transformed into $O^{2-}$, which is absorbed by the solid matrix. In the anode, hydrogen is depleted where water is formed with the $O^{2-}$ ions transferred from the anode electrode. Since ion transfer occurs in solid matrix, continuity equation which is defined for only fluid domain has to be modified. Then appropriate source terms are set in the continuity equation accordingly as;

$R_a = R_{H_2} + R_{H_2O}$ and $R_c = R_{O_2}$, where,

$$R_{H_2} = -i_a/(2F)M_{H_2} \tag{11}$$

$$R_{H_2O} = -i_a/(2F)M_{H_2O} \tag{12}$$

$$R_{O_2} = -i_c/(4F)M_{O_2} \tag{13}$$

$i_{a,c}$ is the exchange current density for anode and cathode, which is explained in the following equations.

### Species balance

Species transport is modeled with Maxwell–Stefan equation;

$$\frac{\partial(\rho\varepsilon w_j)}{\partial t} + \nabla\cdot(J_i + \rho\vec{V}w_i) = R_j \tag{14}$$

where $J_i$ is diffusive flux term and where,

$$J_i = -D_j^{Th}\frac{\nabla T}{T} - \rho w_j\sum_{k=1}^{n}\tilde{D}_{jk}d_k \tag{15}$$

The first term accounts for the effect of temperature gradient on diffusion.

### Momentum balance

Assuming laminar flow in the system, the momentum equations can be expressed as:

$$\frac{d}{dt}(\rho\vec{V}) + \rho\vec{V}\cdot\nabla\vec{V} = \nabla\cdot\left[-pI + \mu\left(\nabla\vec{V} + (\nabla\vec{V})^T\right) - \frac{2\mu}{3}(\nabla\vec{V})I\right] + \rho g \tag{16}$$

where $\mu$ is the viscosity obtained similar to density calculation and $p$ represents the static pressure.

Density of the mixture used in momentum equation as well as in the other equation is calculated via the expression,

$$\rho = \frac{P}{RT}\sum_j x_j M_j \tag{17}$$

where $x_j$ is the mole fraction of the species determined from Maxwell–Stefan equation and $M_j$ is the molecular weight of the species.

Momentum equations is modified with Brinkman Equations;

$$\frac{d}{dt}(\rho\vec{V}/\varepsilon) + \rho\vec{V}\cdot\nabla\vec{V} = \nabla\cdot\left[-pI + \frac{\mu}{\varepsilon}\left(\nabla\vec{V} + (\nabla\vec{V})^T\right) - \frac{2\mu}{3}(\nabla\vec{V})I\right] + \rho g - (\mu/K)\vec{V} + F \tag{18}$$

$(\mu/K)\vec{V}$ is porous media transport in the equation where $K$ is the permeability of the electrode. Source term in Brinkman equation includes the external-force applied to the fluid due to the generation and depletion of the species during the fuel cell reaction as,

$$F = \begin{bmatrix} R_{a,c} & U \\ R_{a,c} & V \end{bmatrix} \tag{19}$$

### Energy balance

The energy conservation equation is.

$$\frac{d(\rho C_p T)}{dt} + \nabla\cdot\left(-k\nabla T + \rho C_p Tu9 + \sum_j h_i N_{D,j}\right) = Q \tag{20}$$

In the equation, $C_p$ specific heat, $k$ is the thermal conductivity and $Q$ denotes the energy due to a source term including joule effect due to ohmic resistance, the electrochemical reactions or radiation according to the domain of interest.

### Electrochemical equations

Electrochemically generated model comprises the following processes:

- Electronic charge balance (Ohm's law)
- Ionic charge balance (Ohm's law)
- Butler–Volmer charge transfer kinetics

*Charge conservation*

The charge is expressed by Ohm's Law and the conservation of charge as follows:

$$\vec{j} = \sigma\nabla\phi \tag{21}$$

$$\frac{\partial\rho_e}{\partial t} + \nabla\cdot\vec{j} = S_c \tag{22}$$

Where is $\vec{j}$, $\sigma$ and $\phi$ are the ionic or electronic current density, the conductivity and the electrical potential. $S_c$ is the charge source term and equal to current density of the considered domain valid only in TPBs, otherwise it is equal to zero. In other words, $S_c$ is equal to the anode or cathode current density calculated from Butler–Volmer equation for the electrodes whereas it is zero for the electrolyte or interconnects purely ionic and purely electronic conductive parts respectively. The electrodes, however, have both ionic and electronic conductivity. Therefore, charge balance equation is required as follows:

$$\vec{j}_{io} = -\vec{j}_{el} \tag{23}$$

*Electrochemical model*

The actual voltage of an SOFC is less than its open circuit voltage owing to irreversible losses:

$$V_{cell} = V - \Delta V_{ohm} - \Delta V_{act} - \Delta V_{con} \tag{24}$$

The current density is by given Butler–Volmer equation:

$$i_{a,c_t} = i_{0,a}\left[\frac{c_{h_2}}{c_{h_2,ref}}\exp\left(\frac{0,5F}{RT}\eta\right) - \frac{c_{h_2o}}{c_{h_2o,ref}}\exp\left(-\frac{1,5F}{RT}\eta\right)\right] \tag{25}$$

where, $i_{0,a}$ anode exchange current density (A/m$^2$), $c_{h_2}$ hydrogen molar concentration, $c_{h_2o}$ water molar concentration, $c_t$ species total molar concentration (mol/m$^3$), $c_{h_2,ref}$ and $c_{h_2o,ref}$ reference concentration (mol/m$^3$), F is faraday constant (C/mol), R universal gas constant (J/(mol K)), T is temperature (K), $\eta$ is loses.

$$i_{c,c_t} = i_{0,c}\left[\exp\left(\frac{3,5F}{RT}\eta\right) - x_{o_2}\frac{c_t}{c_{o_2,ref}}\exp\left(-\frac{0,5F}{RT}\eta\right)\right] \quad (26)$$

where, $i_{0,c}$ is cathode exchange current density (A/m$^2$), $x_{o_2}$ is molar fraction of oxygen.

*Electrochemical reactions*

All electrochemical reactions consist of two separate reactions: an oxidation half-reaction occurring at the anode and reduction half reaction occurring at cathode.

Anode $H_2 + O^{-2} \rightarrow H_2O + 2e^-$ (27)

Cathode $O_2 + 2e^- \rightarrow O^{-2}$ (28)

## Materials and parameters

The mechanical properties of the materials required for the thermo-mechanical stress analysis are summarized in Table 2 [17–20].

## Results and discussion

The calculated stress distributions in the porous Ni–YSZ anode are shown in Figs. 4–8. Figs. 4–6 show the stresses generated as a result of the temperature change from room to 700 °C, 800 °C and 900 °C. When the operation temperature is reduced to 700 °C, the dramatic drop in the stress values is observed as illustrated in Fig. 4. However, stress generation increases at higher temperatures (Figs. 5 and 6). It is seen that at 800 °C, which is an average operation temperature of SOFC, the stress values between the nickel and YSZ phases exceeds 200 MPa even reaches 300 MPa at some regions. Since the material limit for nickel phase is around 317 MPa, this stress level is found to be critical for some locations within the structure.

The calculated thermal stress on the nickel phase which has the highest thermal expansion coefficient is given in Fig. 7. It is seen that the stress generated on the nickel grains is higher than that of YSZ phase due to high thermal conductivity, elasticity modulus and thermal expansion behavior of nickel. On the other hand, the stress level of around 80 MPa is observed within the YSZ phase except the boundaries in contact with the nickel phase (Fig. 8).

According to the obtained results, the delamination of MEA will decrease with especially above 800 °C operation temperature. Simulation studies confirm that the main reason behind this is the delamination between the phases

**Table 2 – The properties of the materials used in the model [17–20].**

| Material | Nickel | 8YSZ | NiO–8YSZ | Ni–8YSZ (reduced) |
|---|---|---|---|---|
| Temperature (K) | 1073 | 1073 | 298 | 298 |
| E (Gpa) | 207 | 157 | 112.3 | 56.8 |
| Poisson ratio (V) | 0.31 | 0.313 | 0.284 | 0.258 |
| Specific heat capacity (J/kg K) | 450 | 460 | – | – |
| Density (kg/m$^3$) | 8800 | 5200 | – | – |
| Thermal conductivity (W/mK) | 60.7 | 2.1 | – | – |
| Thermal expansion coefficient ($\alpha \times 10^{-6}$) | 13.5 | 10.5 | 12.5 | 12.5 |
| Yield strength (Mpa) | 59 | n/a | – | – |
| Tensile strength (Mpa) | 317 | n/a | – | – |

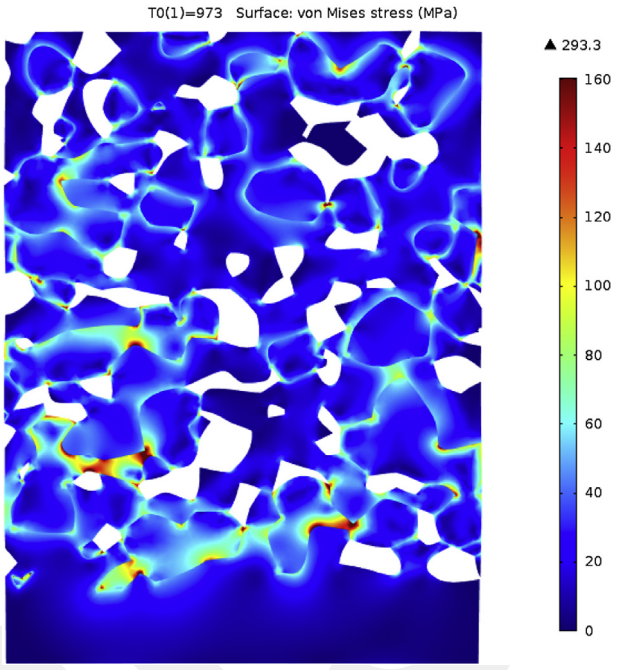


**Fig. 4 – The stress between the Nickel–YSZ at 700 °C.**

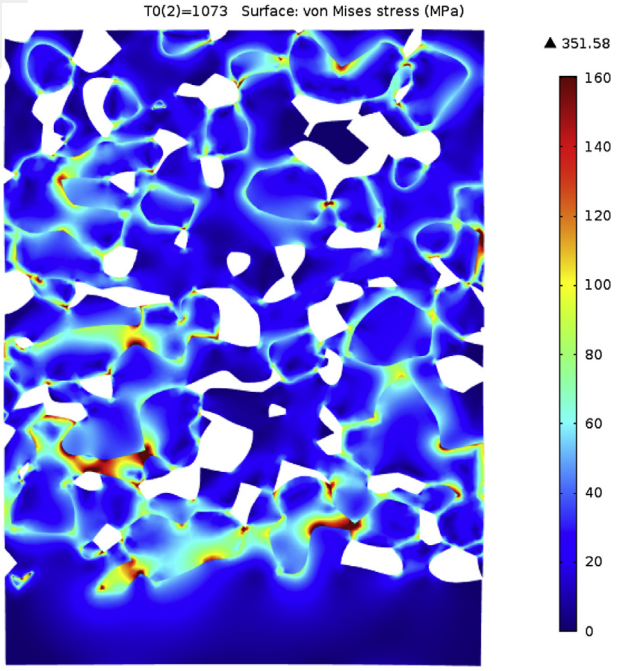


**Fig. 5 – The stress between the Nickel–YSZ at 800 °C.**

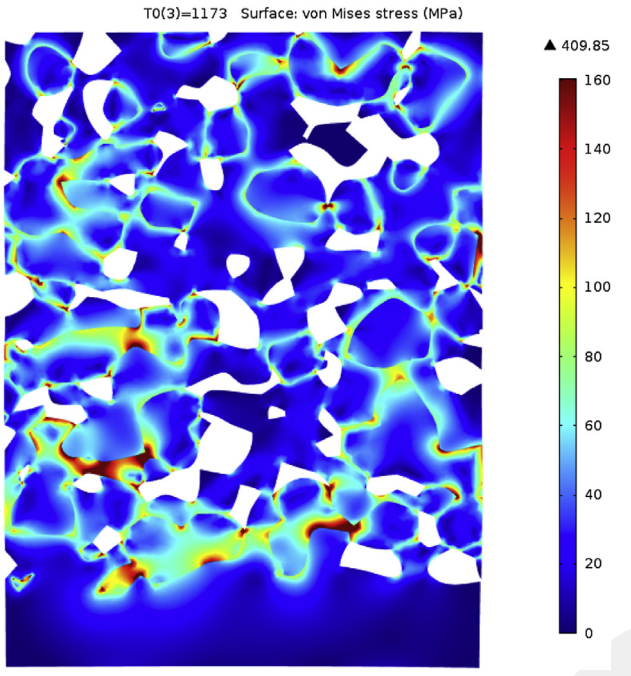


**Fig. 6 – The stress between the Nickel–YSZ at 900 °C.**

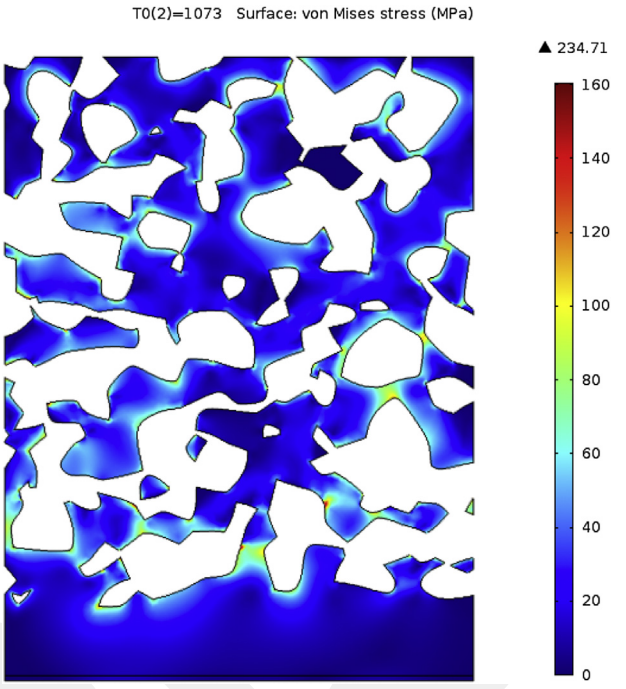


**Fig. 8 – The stress just YSZ phase at 800 °C.**

leading to significant decrease in the number of the triple phase boundaries.

The electrochemical model is also considered in the 2D simulations beside the thermo-mechanical models. Fig. 9 shows the oxide ion transfer pathways within the electrolyte. The most significant parameter affecting the ion distribution is found to be heterogeneous particle distribution. It is seen that there is no ionic paths at some locations resulting in dead zones.

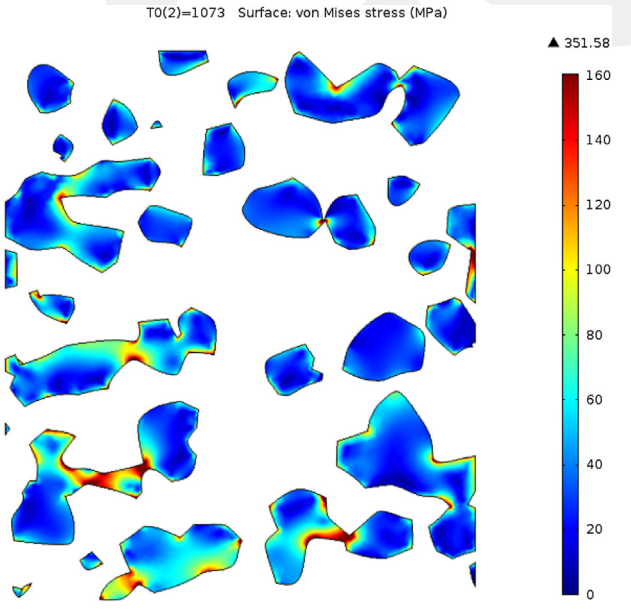


**Fig. 7 – The stress just Nickel phase at 800 °C.**

The ionic current distribution within the electrolyte layer is depicted in Fig. 10 which proves the formation of dead zones. According to the thermo-mechanical analyses, the zones which are more susceptible to failure are also indicated in the figure as "critical region". In case of any mechanical damages within this critical region, no current will be transferred to the upper zones thus new dead zones will be formed. These

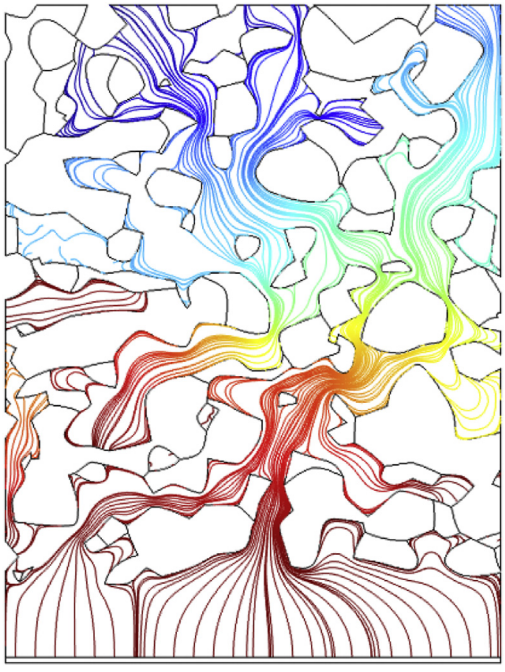

**Fig. 9 – The distribution of ions through the electrolyte path.**

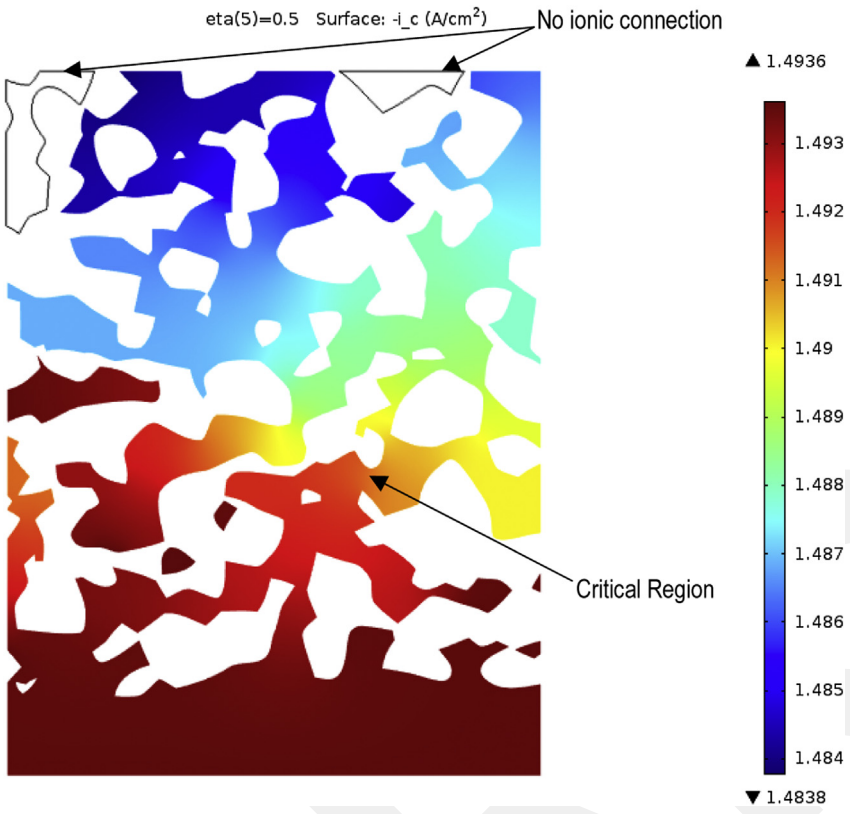


**Fig. 10 – Current distribution through the electrolyte.**

results reveal that the main reason for the performance degradation is mainly reduced oxide ion and electron transfer paths due to damaged triple phase boundaries.

## Conclusions

The thermal stresses inside the solid oxide fuel cell anode microstructure and YSZ electrolyte interface are investigated through 2D micro-scale stress modeling. The calculated results show that at temperatures higher than 800 °C, the generated stress values within the microstructure are higher than the material limits and thus micro-cracks can be developed. These micro-cracks lead to damage in ionic and electronic transfer paths thus leads to reduced number of triple phase boundaries and causes dramatic performance drop. In order to avoid the mechanical damages within the microstructure, the operation temperature should be below 800 °C.

## Nomenclature

| | |
|---|---|
| $\mu$ | viscosity, kg/s m |
| $c_{h_2}$ | hydrogen molar concentration, mol/m$^3$ |
| $c_{h_2,ref}$ | reference concentration, mol/m$^3$ |
| $c_{h_2o}$ | water molar concentration, mol/m$^3$ |
| $c_{h_2o,ref}$ | reference concentration (mol/m$^3$) |
| $C_p$ | specific heat capacity (J/kg K) (J/kg K) |
| $c_t$ | species total molar concentration, mol/m$^3$ |
| $E$ | Young's modulus, GPa |
| $F$ | faraday constant, C/mol |
| FIB | focused ion beam |
| $i_{0,a}$ | anode exchange current density, A/m$^2$ |
| $i_{0,c}$ | cathode exchange current density, A/m$^2$ |
| $j$ | ionic or electronic current density, A/m$^2$ |
| $J_i$ | diffusive flux, m$^2$/s |
| $K$ | permeability of the electrode |
| $k$ | thermal conductivity, W/mK |
| SOFC | solid oxide fuel cell |
| $R$ | universal gas constant, J/(mol K |
| $S_c$ | charge source term |
| SEM | scanning electron microscopy |
| $T$ | temperature, K |
| TEC | thermal expansion coefficient, 1/C |
| $V_{act}$ | activation potential loss, V |
| $V_{cell}$ | cell Voltage, V |
| $V_{con}$ | concentration potential loss, V |
| $V_{ohm}$ | ohmic potential loss, V |
| $x_j$ | mole fraction of the species determined from Maxwell–Stefan equation |
| $x_{o_2}$ | molar fraction of oxygen |
| YSZ | yttrium stabilized zirconia |
| $\varepsilon$ | strain tensor |
| $\beta$ | porosity |
| $\boldsymbol{I}$ | unit tensor |
| $\boldsymbol{f}$ | body force |
| $\boldsymbol{u}$ | displacement vector, m/s |
| $Q$ | joule effect due to ohmic resistance, W |
| $p$ | static pressure, Pa |

| | |
|---|---|
| $\lambda$ | Lame's coefficients |
| $\rho$ | density, kg/m$^3$ |
| $\sigma$ | stress tensor, MPa |
| $\sigma$ | conductivity, S/m |
| $\upsilon$ | Poisson's ratio |
| $\phi$ | electrical potential, V |

## REFERENCES


[1] Singhal SC, Kendall K. High temperature solid oxide fuel cells. 1st ed. 2003. Genova.

[2] Staffell I, Green R. The cost of domestic fuel cell micro-CHP systems. Int J Hydrogen Energy 2013;38:1088–102.

[3] Celik S, Timurkutluk B, Mat MD. Measurement of the temperature distribution in a large solid oxide fuel cell short stack. Int J Hydrogen Energy 2013;38:10534–41.

[4] Gostovic D, Smith JR, Kundinger DP, Jones KS, Wachsman ED. Three-dimensional reconstruction of porous LSCF cathodes. Electrochem Solid State Lett 2007;10:B214–7.

[5] Holzer L, Muench B, Wegmann M, Gasser P, Flatt RJ. FIB-nanotomography of particulate systems – part I: particle shape and topology of interfaces. J Am Ceram Soc 2006;89:2577–85.

[6] Holzer L, Munch B, Iwanschitz B, Cantoni M, Hocker T, Graule T. Quantitative relationships between composition, particle size, triple phase boundary length and surface area in nickel–cermet anodes for solid oxide fuel cells. J Power Sources 2011;196:7076–89.

[7] Kanno D, Shikazono N, Takagi N, Matsuzaki K, Kasagi N. Evaluation of SOFC anode polarization simulation using three-dimensional microstructures reconstructed by FIB tomography. Electrochimica Acta 2011;56:4015–21.

[8] Shearing PR, Cai Q, Golbert JI, Yufit V, Adjiman CS, Brandon NP. Microstructural analysis of a solid oxide fuel cell anode using focused ion beam techniques coupled with electrochemical simulation. J Power Sources 2010;195:4804–10.

[9] Vivet N, Chupin S, Estrade E, Piquero T, Pommier PL, Rochais D, et al. 3D microstructural characterization of a solid oxide fuel cell anode reconstructed by focused ion beam tomography. J Power Sources 2011;196:7541–9.

[10] Vivet N, Chupin S, Estrade E, Richard A, Bonnamy S, Rochais D, et al. Effect of Ni content in SOFC Ni–YSZ cermets: a three-dimensional study by FIB–SEM tomography. J Power Sources 2011;196:9989–97.

[11] Wilson JR, Kobsiriphat W, Mendoza R, Chen HY, Hiller JM, Miller DJ, et al. Three-dimensional reconstruction of a solid-oxide fuel-cell anode. Nat Mater 2006;5:541–4.

[12] Grew KN, Peracchio AA, Chiu WKS. Characterization and analysis methods for the examination of the heterogeneous solid oxide fuel cell electrode microstructure: part 2. Quantitative measurement of the microstructure and contributions to transport losses. J Power Sources 2010;195:7943–58.

[13] Shearing PR, Gelb J, Brandon NP. X-ray nano computerised tomography of SOFC electrodes using a focused ion beam sample-preparation technique. J Eur Ceram Soc 2010;30:1809–14.

[14] Cronin JS, Wilson JR, Barnett SA. Impact of pore microstructure evolution on polarization resistance of Ni-yttria-stabilized zirconia fuel cell anodes. J Power Sources 2011;196:2640–3.

[15] Jasak H, Weller HG. Application of the finite volume method and unstructured meshes to linear elasticity. Int J Numer Meth Eng 2000;48:267–87.

[16] Fryer YD, Bailey C, Cross M, Lai CH. A control volume procedure for solving the elastic stress–strain equations on an unstructured mesh. Appl Math Model 1991;15:639–45.

[17] Atkinson A, Ramos TMGM. Chemically-induced stresses in ceramic oxygen ion-conducting membranes. Solid State Ionics 2000;129:259–69.

[18] Radovic M, Lara-Curzio E. Mechanical properties of tape cast nickel-based anode materials for solid oxide fuel cells before and after reduction in hydrogen. Acta Mater 2004;52:5747–56.

[19] Radovic M, Lara-Curzio E. Elastic properties of nickel-based anodes for solid oxide fuel cells as a function of the fraction of reduced NiO. J Am Ceram Soc 2004;87:2242–6.

[20] Wang L, Wang Y, Zhang WQ, Sun XG, He JQ, Pan ZY, et al. Finite element simulation of stress distribution and development in 8YSZ and double-ceramic-layer $La_2Zr_2O_7$/8YSZ thermal barrier coatings during thermal shock. Appl Surf Sci 2012;258:3540–51.